ACS APPLIED MATERIALS & INTERFACES
Research Article
www.acsami.org

Novel Low Temperature Synthesis Route for Functional Au/ZnFe Mixed Oxide Nanohybrids

Yen Nan Liang,[†,§] Yongmei Li,[†,§] Cindy Ang,[†] Yaodong Shen,[†] Dongzhi Chi,[‡] and Xiao Hu*,[†]

[†]School of Materials Science and Engineering, Nanyang Technological University, Nanyang Avenue, Singapore 639798, Singapore
[‡]Institute of Materials Research and Engineering (IMRE), 3 Research Link, Singapore 117602, Singapore

Supporting Information

ABSTRACT: ZnFe layered double hydroxide (LDH) was synthesized through which the $[AuCl_4]^-$ anions were directly intercalated in situ. Low temperature calcination converts the $[AuCl_4]^-$ intercalated LDH into an intimately mixed ZnFe metal oxides containing favorably dispersed Au nanoparticles. The unique microstructure exhibited substantially improved photocatalytic activity by more than 40 times compared to the baseline material intercalated with $[CO_3]^{2-}$. Such improvement is unprecedented among noble metal decorated photocatalyst materials and is elucidated based on the mechanisms of morphology evolution.

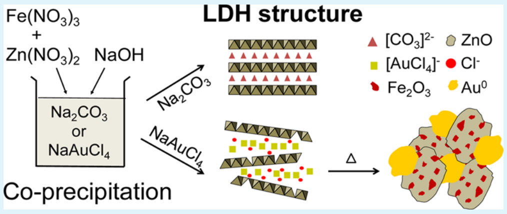

KEYWORDS: *noble metal, intimately mixed metal oxides, photocatalytic activity, low temperature calcination*

1. INTRODUCTION

Noble metals such as Ag, Au, Pt, and Pd are usually incorporated within metal oxide (e.g., TiO_2) as cocatalysts to improve the photocatalytic activity. The improvement is contributed by surface plasmonic resonance (SPR) effects, enhanced visible light absorption, and suppressed electron−hole recombination.[1−3] In the latest study, Bian Z. et al. enhanced the photocatalytic activity of TiO_2 substantially after decoration with Au nanoparticles.[4] Comparing with single phase metal oxide, mixed metal oxides (MMO) combined with noble metal were much less explored in studies of photocatalyst.

MMO can provide multifunctional properties including improved visible light absorption, higher carrier conductivity, and efficient charge transfer due to the existence of heterojunction at the interface.[5,6] Researchers had reported various methods, such as sol−gel,[7] hydrothermal,[6] liquid phase atomic layer deposition (L-ALD),[8] and solution−combustion method,[9] to achieve intimately mixed microstructure of MMO for good photocatalytic performance.

Calcination of layered double hydroxide (LDH) is a facile technique to achieve intimately mixed morphology of MMO. The method has been used to prepare MMO for solar cell[10] and battery applications.[11] LDH, a type of anionic clay with layered brucite-like structure, has a general formula of $M^{2+}{}_{1-x}M^{3+}{}_x(OH)_2(A^{n-})_{x/n}\cdot mH_2O$. M^{2+} and M^{3+} represent divalent and trivalent metallic cations, respectively, while A^{n-} is the interlayer charge compensating anion.[12] Examples of commonly studied LDH include Mg/Al-LDH[13] and Zn/Al-LDH,[14] which are usually prepared by coprecipitation[14,15] and hydrothermal method.[13,16] LDH itself had been reportedly useful for photocatalytic evolution of O_2 and H_2,[17,18] dye degradation,[19] and CO_2 conversion.[20]

Well-dispersed noble metals on LDH[21,22] were usually achieved via reconstruction of LDH,[23] anion exchange,[24] reduction of metallic salts,[25] layer-by-layer assembly,[26] as well as incipient wetness impregnation method.[27] However, good photocatalytic activity of noble-metal/metal-oxide catalyst usually requires high temperature calcination (>500 °C).[27−29] Moreover, all of the above methods are indirect methods which involved the synthesis of LDH before adding noble metals. Direct intercalation of noble metals into LDH interlayer with unique crystallization pathway was not reported before.

In this work, a modified low supersaturation coprecipitation method was used to directly intercalate $[AuCl_4]^-$ into Zn/Fe LDH interlayer. $[CO_3]^{2-}$ intercalated Zn/Fe LDH was also prepared using the same method to serve as baseline references. With $[AuCl_4]^-$ intercalation, the Zn/Fe LDH crystallization pathway was affected and "pseudoamorphous" crystal structures was produced. The photocatalytic activity of the low temperature calcined $[AuCl_4]^-$/ZnFe products showed extraordinary improvement by 43 times compared with calcined $[CO_3]^{2-}$/ZnFe LDH. Discussion will be focused on crystallization and morphological evolution during the in situ intercalation and calcination processes.

2. EXPERIMENTAL SECTION

2.1. Materials and Synthesis. Reagent grade zinc nitrate hexahydrate ($Zn(NO_3)_2\cdot 6H_2O$), iron(III) nitrate nonahydrate ($Fe(NO_3)_3\cdot 9H_2O$), sodium tetrachloroaurate(III) dihydrate ($NaAuCl_4\cdot 2H_2O$), sodium carbonate (Na_2CO_3), and methylene blue (MB) were purchased from Sigma-Aldrich and used without further purification.

Received: April 15, 2014
Accepted: July 28, 2014
Published: July 28, 2014

dx.doi.org/10.1021/am502256e | *ACS Appl. Mater. Interfaces* 2014, 6, 12406−12412

For $[AuCl_4]^-$/ZnFe LDH synthesis, precursors, that is, $Zn(NO_3)_2 \cdot 6H_2O$ and $Fe(NO_3)_3 \cdot 9H_2O$, were coprecipitated in an aqueous solution containing $NaAuCl_4 \cdot 2H_2O$. The molar ratio of Zn/Fe/Au was fixed at 3:1:2, and the reaction solution pH was maintained at 10. After all the precursors were added, the reaction solution was sealed and stirred for 18 h. The as-prepared solid products were then purified by filtering with DI water, until the filtrate solution reached pH = 7. After drying at 90 °C, the clustered powdery products were ground into finer form and used for further characterizations. Low temperature calcination of the as-prepared products at 200 and 300 °C for 5 h were carried out and denoted as $[AuCl_4]^-$/ZnFe (200 °C) and $[AuCl_4]^-$/ZnFe (300 °C), respectively. For $[CO_3]^{2-}$/ZnFe LDH synthesis, the procedures were the same, except for the replacement of $NaAuCl_4 \cdot 2H_2O$ with Na_2CO_3. Calcined $[CO_3]^{2-}$/ZnFe LDH at 200 and 300 °C are denoted as $[CO_3]^{2-}$/ZnFe (200 °C) and $[CO_3]^{2-}$/ZnFe (300 °C), respectively.

2.2. Photocatalytic Test. The organic dye solution used for photocatalytic test was 10^{-5} M methylene blue (MB) solution which is within the measurement range of the absorption spectroscopy. The catalyst concentration is 0.7 mg/mL at which the solution is stable and homogeneously dispersed. For photocatalytic reactions, 30 mL solution of each sample was prepared. Before photocatalytic tests, all the samples were kept in dark for 2 h to allow complete dyes adsorption onto the synthesized products. Irradiation was done with solar simulator (Newport model 66902, intensity = 100 mW/cm^2) with simultaneous O_2 bubbling and stirring to ensure homogeneous mixing. The extent of photocatalytic degradation of MB was studied by measuring absorption of solutions at different irradiation intervals.

2.3. Characterizations. Morphology of synthesized products were observed using transmission electron microscopy (TEM) by JEOL 2100F. Powder X-ray diffraction (XRD) was performed by Shimadzu XRD-600 diffractometer with Cu−Kα radiation source (λ = 1.54 Å) using measurement step-size of 0.02° and scan-rate of 2°/min. Energy dispersive X-ray spectroscopy (EDX) was done using transmission electron microscope (JEOL 2100F) equipped with EDX detector. Shimadzu UV 2501PC UV−vis spectrophotometer was used to measure absorption of synthesized products and photocatalytic test samples. Thermogravimetric analysis (TGA) was carried out using TA Q500 that provided information on weight loss during constant-rate heating test (heating rate = 8 °C/min) under atmosphere of synthetic air.

3. RESULTS AND DISCUSSION

3.1. Structural Properties of $[CO_3]^{2-}$/ZnFe LDH and $[AuCl_4]^-$/ZnFe LDH. The XRD spectra of as prepared $[CO_3]^{2-}$/ZnFe LDH and $[AuCl_4]^-$/ZnFe LDH are shown in Figure 1. For as-prepared $[CO_3]^{2-}$/ZnFe LDH, the diffraction peak at 12° corresponds to a d_{003} spacing of 7.38 Å (spectrum i in Figure 1). This is attributed to the intercalated $[CO_3]^{2-}$ (planar diagonal structure with diameter ∼2.4 Å) within LDH layers.

Interestingly, for as-prepared $[AuCl_4]^-$/ZnFe LDH, XRD spectrum showing "pseudoamorphous" microstructure, that is, phase containing plane-crystals that are too thin or small for effective diffraction of incident X-ray, reflected as a broad diffraction hump at the 2θ region of 30° to 40° (spectrum ii in Figure 1). This is based on the fact that there is no distinct characteristic LDH peak for as-prepared $[AuCl_4]^-$/ZnFe LDH despite the clearly observed LDH crystals in TEM images (Figure 2b). The broad diffraction "hump" indicates a broad distribution of lattice parameters. More information on the microstructure and morphology are obtained from the TEM images.

Shown in Figure 2 are the morphologies of as prepared $[CO_3]^{2-}$/ZnFe LDH and $[AuCl_4]^-$/ZnFe LDH (see Supporting Information (SI), Figure S1 for corresponding global views). For as-prepared $[CO_3]^{2-}$/ZnFe LDH, planar and edged crystals with good size uniformity can be observed (Figure 2a). The *d*-spacing is measured to be 0.29 nm. Estimated from the global views (SI Figure S1), the diameter of the layered crystals is between 5 and 15 nm (centered at about 10 nm).

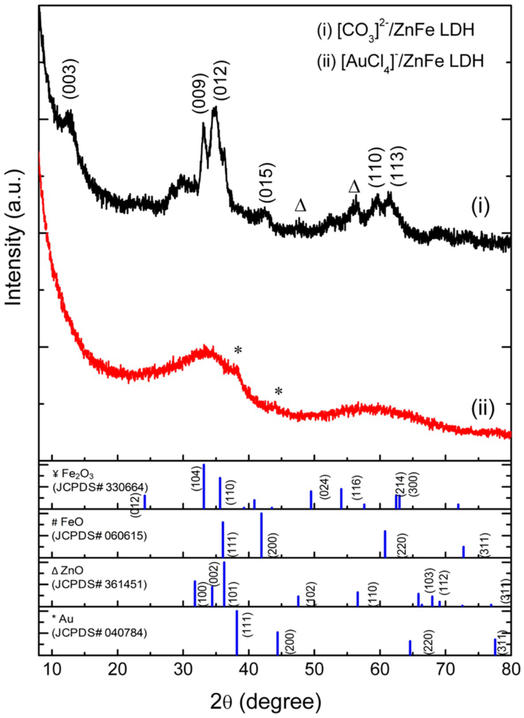

Figure 1. Powder XRD spectra of as prepared $[CO_3]^{2-}$/ZnFe LDH and $[AuCl_4]^-$/ZnFe LDH. The reference XRD spectra of standard Au, ZnO, FeO, and Fe_2O_3 are included for comparison.

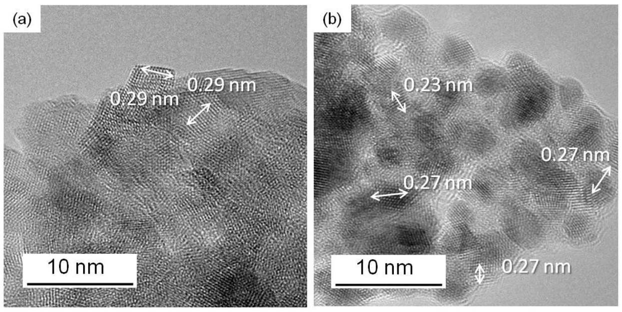

Figure 2. Morphology of (a) $[CO_3]^{2-}$/ZnFe LDH and (b) $[AuCl_4]^-$/ZnFe LDH. The *d*-spacings of 0.27, 0.29, and 0.23 nm belonged to $[CO_3]^{2-}$/ZnFe LDH, $[AuCl_4]^-$/ZnFe LDH, and Au^0, respectively.

With the presence of $[AuCl_4]^-$, expanded and irregular LDH crystals are observed together with higher contrast regions. The higher contrast regions in TEM images were contributed by the Au species (similar to "staining" effect by heavy atoms) (Figure 2b). Such contrast was helpful in identifying regions that were spatially rich of Au species. As observed from the global views of the $[AuCl_4]^-$/ZnFe LDH (see Supporting Information, Figure S1-bi), Au species were well-dispersed within the synthesized products.

Although the XRD spectrum of the as-prepared $[AuCl_4]^-$/ZnFe LDH shows a "pseudoamorphous" phase, nanocrystals are clearly observed under TEM (Figure 2b). The crystals are not randomly distributed but are mixed intimately with Au species. By analyzing the *d*-spacing, besides a few Au^0 crystals with *d*-spacing of 0.23 nm corresponding to (111) crystal plane

Scheme 1. Illustrations of Morphology Evolution of (a) $[CO_3]^{2-}$/ZnFe LDH and $[AuCl_4]^-$/ZnFe LDH Structures and (b) MMO Structures after Calcination

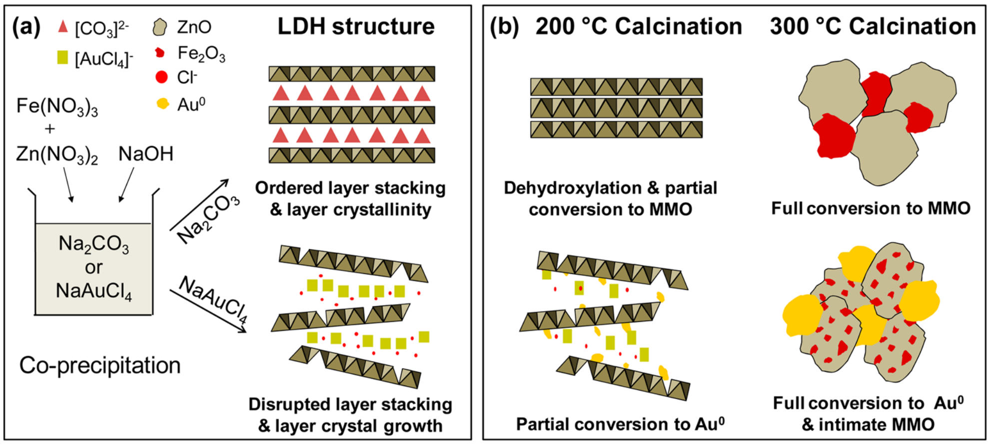

(caused by 90 °C drying condition), most of the crystals found are with *d*-spacing around 0.27 nm. The crystals could be confirmed as LDH with $[AuCl_4]^-$ or hydrolyzed $[AuCl_4]^-$ species as intercalating agent. The evidence of decreased *d*-spacing from ~0.29 nm (with $[CO_3]^{2-}$ intercalation) to ~0.27 nm and the lack of detection of (003) peak in XRD spectrum shows disruption of both layered crystal growth and layer stacking in $[AuCl_4]^-$/ZnFe LDH structure formation.

In comparison to $[CO_3]^{2-}$ intercalation, disrupted LDH structure is a result of direct intercalation of $[AuCl_4]^-$. Scheme 1a illustrates the different formation mechanisms of the two structures. The top right graph of Scheme 1a shows a well crystallized and ordered layer stacking for $[CO_3]^{2-}$/ZnFe LDH. With $[AuCl_4]^-$ intercalation, both of the layered crystallization and the layer stacking were disrupted (bottom right graph of Scheme 1a). The disruption is believed to be contributed by the in situ synthesis process that gave rise to strong interactions (electrostatic and hydrogen bonding) between the counter anions $[AuCl_4]^-$ and metal cation layers Zn^{2+} and Fe^{3+}. In addition, the disruption could come from the hydrolysis of $[AuCl_4]^-$, which generated $[AuCl_4]^-$, $[Au(OH)Cl_3]^-$, $[Au(OH)_2Cl_2]^-$, $[Au(OH)_3Cl]^-$, and Cl^-. The detailed intercalation mechanisms of this system are worthy of further study. Scheme 1b illustrates the MMO structure of $[CO_3]^{2-}$ and $[AuCl_4]^-$ intercalated ZnFe LDH after calcination, which will be discussed in the following section.

3.2. Structural Properties of $[CO_3]^{2-}$/ZnFe LDH and $[AuCl_4]^-$/ZnFe LDH after Calcination.

3.2.1. Thermogravimetric Properties of $[CO_3]^{2-}$/ZnFe LDH and $[AuCl_4]^-$/ZnFe LDH. TGA results, providing information on weight change of as-prepared $[CO_3]^{2-}$/ZnFe LDH and $[AuCl_4]^-$/ZnFe LDH with increasing temperature, are essential for studying evolutions of morphologies, compositions, and crystal phases. Figure 3 shows the TGA curves of the as-prepared $[CO_3]^{2-}$/ZnFe LDH and $[AuCl_4]^-$/ZnFe LDH. It can be seen for each of them, the weight losses happened at distinctly different temperature ranges.

For as-prepared $[CO_3]^{2-}$/ZnFe LDH, the first stage weight loss of adsorbed and interlayer water happened at ~100 °C, and the subsequent second stage weight loss is due to two overlapping events of dehydroxylation and anion decomposition occurred at ~240 °C. However, the as-prepared $[AuCl_4]^-$/ZnFe LDH exhibited a delayed and much slower weight loss profile upon calcination. The first stage loss of adsorbed and interlayer water was delayed until 140 °C. Even at 200 °C, $[AuCl_4]^-$/ZnFe LDH had barely undergone the dehydroxylation process. At 300 °C, $[AuCl_4]^-$/ZnFe LDH experienced larger extent of dehydroxylation and $[AuCl_4]^-$ decomposition. Collapse of LDH structure was substantially delayed until 410 °C. It should be highlighted that the delayed thermal decomposition behavior is consistent with successful $[AuCl_4]^-$ intercalation. First, $[AuCl_4]^-$ possesses much lower volatility than $[CO_3]^{2-}$. Second, the strong interaction between the $[AuCl_4]^-$ and the LDH layers also contribute to the delayed decomposition process. Furthermore, the decomposition of $[AuCl_4]^-$ lead to release of Cl_2 and growth of Au nanoparticles, which inhibit merging of LDH layers into agglomerated MMO.

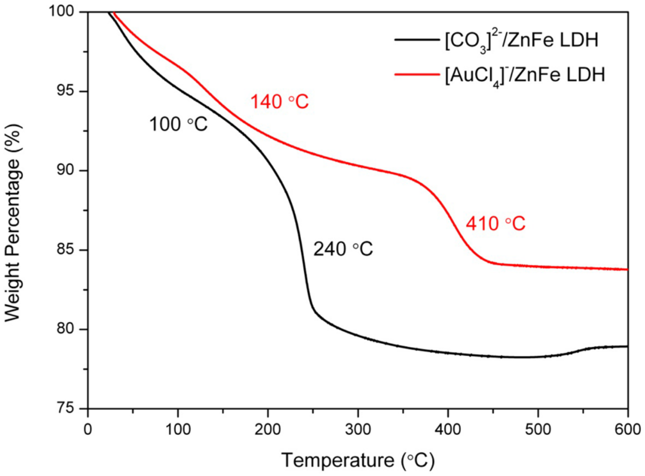

Figure 3. Thermogravimetric properties of as-prepared $[CO_3]^{2-}$/ZnFe LDH and $[AuCl_4]^-$/ZnFe LDH.

As seen from spectra i and ii in Figure 4, the disappearance of (003) peak at 12° in $[CO_3]^{2-}$/ZnFe (200 °C) and $[CO_3]^{2-}$/ZnFe (300 °C) indicates the collapse of LDH structure. The emergence of diffraction peaks assignable to ZnO, FeO, and Fe_2O_3 indicates the formation of MMO. ZnO (100) crystallite size is 15.4 nm, as calculated using the Sherrer's equation.

For $[AuCl_4]^-$/ZnFe LDH samples, the XRD spectra indicate growth of gold nanoparticles when calcined at both 200 and 300 °C calcination (spectra iii and iv in Figure 4), although MMO only formed during calcination at 300 °C. Based on the Scherrer's equation, Au crystallite size is 9.2 nm, and ZnO

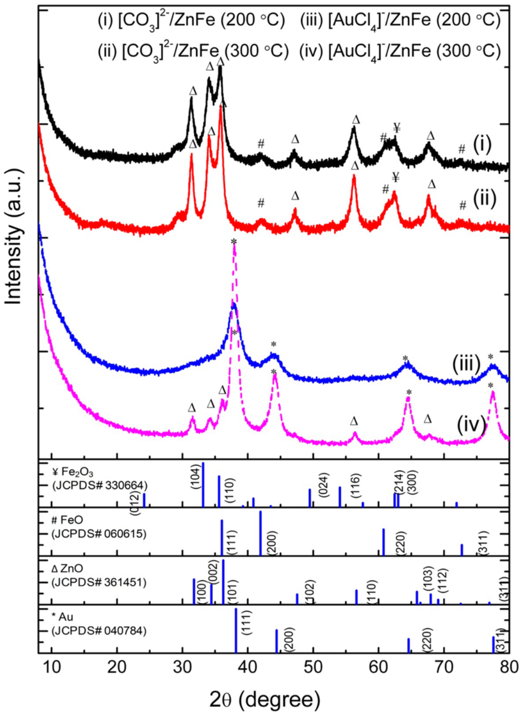

Figure 4. Powder XRD spectra of $[CO_3]^{2-}$/ZnFe (200 °C), $[CO_3]^{2-}$/ZnFe (300 °C), $[AuCl_4]^{-}$/ZnFe (200 °C), and $[AuCl_4]^{-}$/ZnFe (300 °C). The reference XRD spectra of standard Au, ZnO, FeO, and Fe_2O_3 are included for comparison.

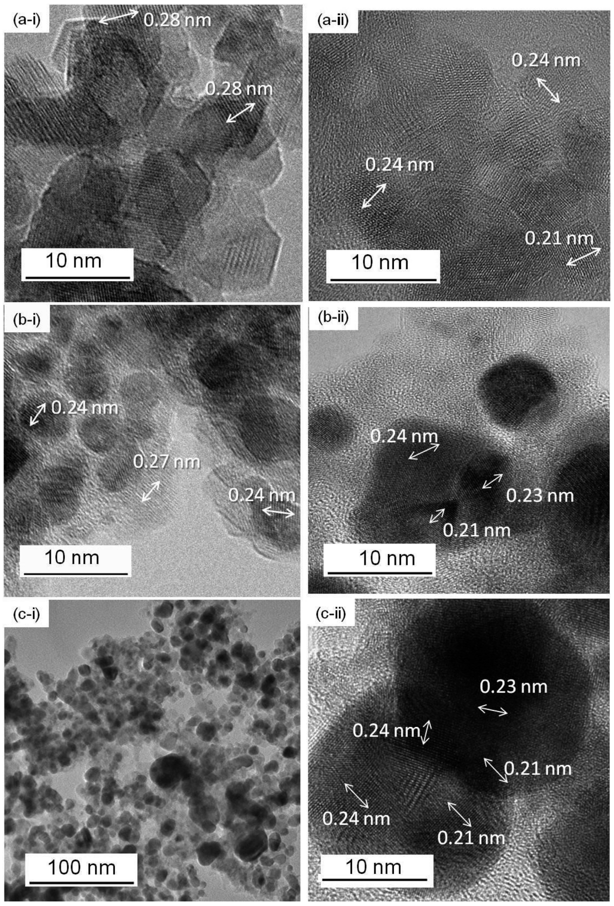

Figure 5. Morphologies of (a-i) $[CO_3]^{2-}$/ZnFe (200 °C), (a-ii) $[CO_3]^{2-}$/ZnFe (300 °C); (b-i) $[AuCl_4]^{-}$/ZnFe (200 °C), (b-ii) $[AuCl_4]^{-}$/ZnFe (300 °C). (c-i and c-ii) Low and high magnification views of $[AuCl_4]^{-}$/ZnFe (300 °C). The *d*-spacings of ∼0.27, 0.21, 0.23, 0.24, and 0.28 nm belong to $[AuCl_4]^{-}$/ZnFe LDH structures, Fe_2O_3 (202), Au^0 (111), ZnO (101), and ZnO (100), respectively.

crystallite size is 10.8 nm. This result is consistent with TGA results that show gradual dehydroxylation at 300 °C calcination. Iron oxide diffraction is not seen in $[AuCl_4]^{-}$/ZnFe (300 °C) XRD spectrum due to even smaller size than that of ZnO, which poorly diffract incident X-ray. The TEM images of calcined $[CO_3]^{2-}$/ZnFe LDH and $[AuCl_4]^{-}$/ZnFe LDH further corroborated our proposed crystallization schemes.

3.2.2. Morphology of $[CO_3]^{2-}$/ZnFe LDH and $[AuCl_4]^{-}$/ZnFe LDH after Calcination. Different morphologies of calcined $[CO_3]^{2-}$/ZnFe LDH and $[AuCl_4]^{-}$/ZnFe LDH are shown in the TEM images in Figure 5. For $[CO_3]^{2-}$/ZnFe LDH, hexagonal morphology is retained after 200 °C calcination (Figure 5a-i), although the XRD spectrum (Figure 4i) shows conversion to MMO crystal phase. The hexagonal structures further collapsed and agglomerated after 300 °C calcination (Figure 5a-ii). The measured *d*-spacings are 0.24 and 0.21 nm, which correspond to ZnO (101) and Fe_2O_3 (202), respectively.

For $[AuCl_4]^{-}$/ZnFe LDH, further calcination at 200 and 300 °C rendered the Au nanoparticles to grow and became more structurally defined. TEM image (Figure 5b-i) shows $[AuCl_4]^{-}$/ZnFe (200 °C) are still in planar structure. The majority *d*-spacings of large-size crystals measured are 0.27 nm indicating LDH structure. Partial conversion of charge-balance ion, that is, $[AuCl_4]^{-}$ to Au^0 was found. Only very few small sized ZnO crystals can be seen under TEM in this case. This is also consistent with the XRD result (Figure 4iii) where ZnO crystals still cannot be seen. Upon 300 °C calcination, as shown in the TEM images of Figure 5b-ii and c-ii, all $[AuCl_4]^{-}$ converted to Au nanoparticles (0.23 nm), and LDH layers dehydroxylated and converted to intimately mixed ZnO (0.24 nm) and Fe_2O_3 (0.21 nm). In addition, the TEM images show that ZnO, Fe_2O_3, and Au particles coexisted as an intimately mixed unit (Figure 5c-ii), lower magnification TEM image (Figure 5c-i) shows that the intimately MMO units are well dispersed.

Based on the above discussion, Scheme 1b is proposed to illustrate the morphology evolution of calcined $[CO_3]^{2-}$/ZnFe LDH and $[AuCl_4]^{-}$/ZnFe LDH. With $[CO_3]^{2-}$ intercalation, the anionic balancing ion decomposed and LDH layer merged at 200 °C calcination. Calcination at 300 °C led to the growth of MMO through interlayer merging of metal ions. With $[AuCl_4]^{-}$ intercalation, the decomposition is understandably delayed. Gradual conversion of charge-balance ion ($[AuCl_4]^{-}$) to Au nanoparticles occurred prior to the growth of MMO. The partially converted Au nanoparticles were deposited on LDH layers as shown in Scheme 1b for $[AuCl_4]^{-}$/ZnFe (200 °C). Due to the presence of Au, interlayer merging became more difficult during calcination. Any growth of MMO took place mainly through intralayer merging of metal ions instead of interlayer merging as in the case of $[CO_3]^{2-}$/ZnFe (300 °C). Based on this understanding, the morphology evolution of $[CO_3]^{2-}$/ZnFe (300 °C) and $[AuCl_4]^{-}$/ZnFe (300 °C) is also explained in Scheme 1b.

The differences in morphology evolution during crystallization and calcination for $[CO_3]^{2-}$/ZnFe LDH and $[AuCl_4]^{-}$/ZnFe LDH are reflected in two aspects. First, compared with $[CO_3]^{2-}$/ZnFe (300 °C), the oxide particle size is smaller for

$[AuCl_4]^-$/ZnFe (300 °C) due to less Zn and Fe cations available during intralayer merging process, as interlayer growth is hindered by Au. Applying the Scherrer's equation to ZnO (100) peak, smaller crystallite size (10.8 nm) was calculated for $[AuCl_4]^-$/ZnFe (300 °C) than to that of $[CO_3]^{2-}$/ZnFe (300 °C) (15.4 nm). Second, the particle assembly is different as illustrated in Scheme 1b. The top right graph illustrates the particle assembly for $[CO_3]^{2-}$/ZnFe (300 °C) by interlayer merging growth process. However, the intralayer merging growth process, as in the case of $[AuCl_4]^-$/ZnFe (300 °C), can lead to iron oxide existing with even smaller size than surrounding zinc oxide particle, as illustrated by the bottom right graph in Scheme 1b. The existence of iron oxide is supported by the EDX spectrum that confirms a Zn to Fe ratio of 3:1 (SI Figure S2), and also by the *d*-spacing of 0.21 nm seen under TEM that belongs to Fe_2O_3 (Figure 5b-ii, c-ii). While the absence of detectable FeO or Fe_2O_3 by XRD further proves their smaller size (Figure 4iv).

Photocatalytic Activity of $[CO_3]^{2-}$/ZnFe LDH, and $[AuCl_4]^-$/ZnFe LDH Based Samples. Zn/Fe LDH was reported to be very useful for photodegradation of azo dyes.[30] Zn/Fe MMO also showed good potential for photocatalytic degradation of dyes and H_2 evolution.[9] In this work, the $[CO_3]^{2-}$/ZnFe LDH and $[AuCl_4]^-$/ZnFe LDH based samples had been employed for photocatalytic degradation of MB. MB was typically used in studies of wastewater treatment relevant to organic dyes pollution. Bubbling of O_2 is needed to help produce O_2^-• and OH•, which promote the degradation of MB. The results of photocatalytic degradation of MB in the presence of $[CO_3]^{2-}$/ZnFe LDH and $[AuCl_4]^-$/ZnFe LDH based samples are presented in Figure 6.

It can be observed in Figure 6 that both as-prepared and calcined $[CO_3]^{2-}$/ZnFe LDH exhibited poor photocatalytic activity. For as-prepared $[AuCl_4]^-$/ZnFe LDH, significantly improved photocatalytic activity can already be seen without calcination. Calcination at 300 °C further substantially improved its photocatalytic activity. The photocatalysis rate can be estimated using the slope of the normalized intensity curves at zero time. Using the slope of as-prepared $[CO_3]^{2-}$/ZnFe LDH as baseline, 3.5 and 5 times enhancements could be achieved for $[CO_3]^{2-}$/ZnFe (200 °C) and $[CO_3]^{2-}$/ZnFe (300 °C), respectively. For as-prepared $[AuCl_4]^-$/ZnFe LDH, $[AuCl_4]^-$/ZnFe (200 °C), and $[AuCl_4]^-$/ZnFe (300 °C), 32, 33, and 43 times enhancements were achieved, respectively. The pseudo-first-order kinetic equation $\ln(A_0/A) = kt$ has also been applied, and the k values are given inside Figure 6. Higher calcination temperature (>300 °C) for $[AuCl_4]^-$/ZnFe LDH is believed to be detrimental to the photocatalytic activity due to uncontrolled growth and agglomeration of mixed oxides.

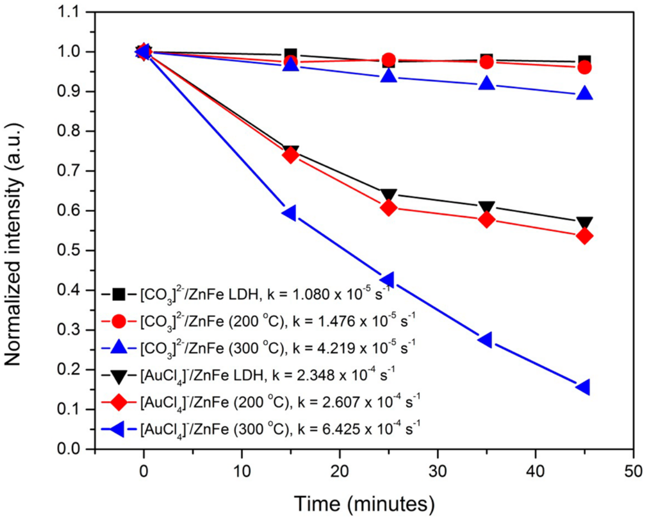

Figure 6. Absorbance change of methylene blue dye solutions, which shows the photocatalytic activity of $[CO_3]^{2-}$/ZnFe LDH, $[CO_3]^{2-}$/ZnFe (200 °C), $[CO_3]^{2-}$/ZnFe (300 °C), $[AuCl_4]^-$/ZnFe LDH, $[AuCl_4]^-$/ZnFe (200 °C), and $[AuCl_4]^-$/ZnFe (300 °C). k is the reaction rate constant determined based on pseudo-first-order kinetics.

UV–vis absorption is one of the major factors that determine the efficiency of electron–hole pair generation. Figure 7 shows the absorption spectra of $[CO_3]^{2-}$/ZnFe LDH and $[AuCl_4]^-$/ZnFe LDH based samples. It can be seen that calcination results in clearer characteristic ZnO band-edge absorption for both set of samples. Furthermore, $[AuCl_4]^-$/ZnFe (200 °C) and $[AuCl_4]^-$/ZnFe (300 °C) exhibit improved visible-light absorption that is beneficial for photocatalytic application, since an AM1.5G solar simulator was used in our photocatalytic tests.

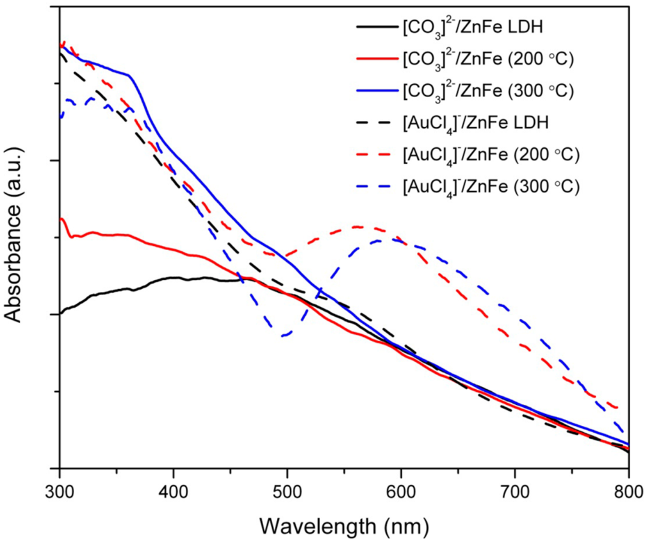

Figure 7. Absorption spectra of $[CO_3]^{2-}$/ZnFe LDH, $[CO_3]^{2-}$/ZnFe (200 °C), $[CO_3]^{2-}$/ZnFe (300 °C), $[AuCl_4]^-$/ZnFe LDH, $[AuCl_4]^-$/ZnFe (200 °C), and $[AuCl_4]^-$/ZnFe (300 °C). An improved absorbance in high wavelength region can be achieved with the incorporation of Au species after calcination.

Au is known to improve photocatalytic reaction. The SPR effect created electron excitation upon plasmonic band absorption,[1] enhance the visible light absorption of low band gap semiconductor[31] and UV light absorption of high band gap semiconductor.[32] Besides that, the favored electron capture by Au species suppressed electron–hole recombination. Recently reported photocatalytic enhancement of TiO_2 by noble metals was 29 times,[4] whereas, up to 43 times of enhancement was achieved in our system. In addition to the reasons mentioned above, it is necessary to emphasize that the manifestation of greatly enhanced photocatalytic activity in our system critically relied on the intimately mixed morphology created.

Scheme 2a illustrates the charge transfer across the band potentials of MMO. This band energy configuration favors charge transfer within the MMO. Upon light absorption, the excited electrons can be transferred from Fe_2O_3 to ZnO, and

Scheme 2. Schematic Representation of (a) charge Transfer Across the Band Gap Structure and (b) Synergetic Interactions between Metal Oxides of $[AuCl_4]^-$/ZnFe (300 °C)

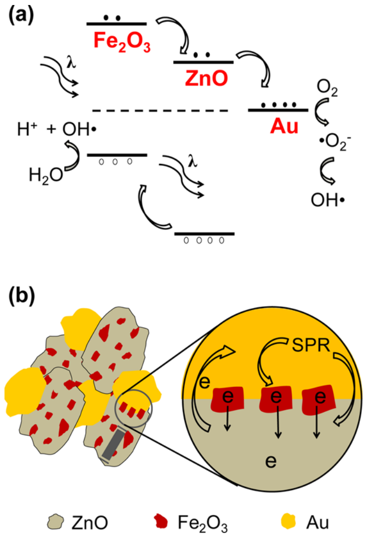

finally captured by Au nanoparticles to create O_2^-● free radical. In the meantime, photo generated holes are transferred to Fe_2O_3 and finally captured to generate OH● radicals that degrade the MB dye.

Scheme 2b illustrated the synergetic interactions within metal oxides as well as Au nanoparticle in $[AuCl_4]^-$/ZnFe (300 °C). The SPR of Au nanoparticles improves the light absorption of Fe_2O_3 and ZnO. Excited electrons are efficiently transferred from the excitation sites to avoid recombination and finally captured by Au nanoparticles for photocatalytic reactions. Intimately mixed morphology in these hybrids improved the efficiency of the overall processes and maximized the number of reaction sites.

4. CONCLUSIONS

In this work, $[AuCl_4]^-$ was directly intercalated into ZnFe LDH structure by a coprecipitation method. During low temperature calcination, the intercalated charge-balance $[AuCl_4]^-$ ions were converted to Au nanoparticles before decomposition of LDH layers, and hindered the interlayer merging. Further calcination led to MMO growth through an intralayer merging growth mechanism. Comparing with $[CO_3]^{2-}$/ZnFe LDH, low temperature calcined $[AuCl_4]^-$/ZnFe LDH at 300 °C exhibited 43 times improvement in photocatalytic activities. The significant improvement of photocatalytic performance is attributed to the novel morphology, which ensures the synergetic interactions between metal oxides and greatly manifested the role of Au nanoparticles. The concept and methodology employed in this work are believed to be extendable to other noble metals and LDH material systems.

■ ASSOCIATED CONTENT

Ⓢ Supporting Information

TEM images showing the global views of $[CO_3]^{2-}$/ZnFe and $[AuCl_4]^-$/ZnFe based samples; EDX spectrum of $[AuCl_4]^-$/ZnFe (300 °C). This material is available free of charge via the Internet at http://pubs.acs.org.

■ AUTHOR INFORMATION

Corresponding Author

*Tel: 65 6790 4610. Fax: 65 6790 9081. Email: asxhu@ntu.edu.sg.

Author Contributions

[§]Equal first author contribution from Y.N. Liang and Y. Li. The manuscript was written through contributions of all authors. X. Hu oversaw the research work. All authors have given approval to the final version of the manuscript.

Funding

The authors acknowledge National Research Foundation (NRF) and A-Star Singapore for support under the MIMO program.

Notes

The authors declare no competing financial interest.

■ ACKNOWLEDGMENTS

The TEM, XRD, and EDX works were performed at the Facility for Analysis, Characterization, Testing, and Simulation (FACTS) in Nanyang Technological University, Singapore.

■ ABBREVIATIONS

LDH, layer-double-hydroxide
MMO, mixed metal oxide
SPR, surface plasmonic resonant
TEM, transmission electron microscopy
XRD, X-ray diffraction
EDX, energy-dispersive X-ray spectroscopy
MB, methylene blue

■ REFERENCES

(1) Silva, C. G.; Juárez, R.; Marino, T.; Molinari, R.; García, H. Influence of Excitation Wavelength (UV or Visible Light) on the Photocatalytic Activity of Titania Containing Gold Nanoparticles for the Generation of Hydrogen or Oxygen from Water. *J. Am. Chem. Soc.* **2010**, *133*, 595−602.

(2) Ismail, A. A.; Bahnemann, D. W.; Bannat, I.; Wark, M. Gold Nanoparticles on Mesoporous Interparticle Networks of Titanium Dioxide Nanocrystals for Enhanced Photonic Efficiencies. *J. Phys. Chem. C* **2009**, *113*, 7429−7435.

(3) Wang, N.; Tachikawa, T.; Majima, T. Single-Molecule, Single-Particle Observation of Size-Dependent Photocatalytic Activity in Au/TiO_2 Nanocomposites. *Chem. Sci.* **2011**, *2*, 891−900.

(4) Bian, Z.; Tachikawa, T.; Zhang, P.; Fujitsuka, M.; Majima, T. Au/TiO_2 Superstructure-Based Plasmonic Photocatalysts Exhibiting Efficient Charge Separation and Unprecedented Activity. *J. Am. Chem. Soc.* **2014**, *136*, 458−465.

(5) Kawahara, T.; Konishi, Y.; Tada, H.; Tohge, N.; Ito, S. Patterned TiO_2/SnO_2 Bilayer Type Photocatalyst. 2. Efficient Dehydrogenation of Methanol. *Langmuir* **2001**, *17*, 7442−7445.

(6) Uddin, M. T.; Nicolas, Y.; Olivier, C.; Toupance, T.; Servant, L.; Muller, M. M.; Kleebe, H. J.; Ziegler, J.; Jaegermann, W. Nanostructured SnO_2−ZnO Heterojunction Photocatalysts Showing Enhanced Photocatalytic Activity for the Degradation of Organic Dyes. *Inorg. Chem.* **2012**, *51*, 7764−7773.

(7) Tripathi, A. M.; Nair, R. G.; Samdarshi, S. K. Visible Active Silver Sensitized Vanadium Titanium Mixed Metal Oxide Photocatalyst Nanoparticles through Sol−Gel Technique. *Sol. Energy Mater. Sol. Cells* **2010**, *94*, 2379−2385.

(8) Shen, Y.; Foong, T. R. B.; Hu, X. Towards Atomic Level Vanadium Doping of TiO_2 via Liquid-Phase Atomic Layer Deposition. *Appl. Catal., A* **2011**, *409−410*, 87−90.

(9) Pradhan, G. K.; Martha, S.; Parida, K. M. Synthesis of Multifunctional Nanostructured Zinc−Iron Mixed Oxide Photo-

catalyst by a Simple Solution-Combustion Technique. *ACS Appl. Mater. Interfaces* **2011**, *4*, 707−713.

(10) Teruel, L.; Bouizi, Y.; Atienzar, P.; Fornes, V.; Garcia, H. Hydrotalcites of Zinc and Titanium as Precursors of Finely Dispersed Mixed Oxide Semiconductors for Dye-Sensitized Solar Cells. *Energy Environ. Sci.* **2010**, *3*, 154−159.

(11) Latorre-Sanchez, M.; Atienzar, P.; Abellan, G.; Puche, M.; Fornes, V.; Ribera, A.; Garcia, H. The Synthesis of a Hybrid Graphene−Nickel/Manganese Mixed Oxide and Its Performance in Lithium-Ion Batteries. *Carbon* **2012**, *50*, 518−525.

(12) Evans, D. G.; Slade, R. C. T. In *Structure and Bonding, Structural Aspects of Layered Double Hydroxides*, Springer-Verlag: Berlin Heidelberg, 2006; Chapter 1, pp 1−87.

(13) Xu, Z. P.; Lu, G. Q. Hydrothermal Synthesis of Layered Double Hydroxides (LDHs) from Mixed MgO and Al_2O_3: LDH Formation Mechanism. *Chem. Mater.* **2005**, *17*, 1055−1062.

(14) Patzkó, Á.; Kun, R.; Hornok, V.; Dékány, I.; Engelhardt, T.; Schall, N. ZnAl-Layer Double Hydroxides as Photocatalysts for Oxidation of Phenol in Aqueous Solution. *Colloids Surf., A* **2005**, *265*, 64−72.

(15) Silva, C. G.; Bouizi, Y.; Fornés, V.; García, H. Layered Double Hydroxides as Highly Efficient Photocatalysts for Visible Light Oxygen Generation from Water. *J. Am. Chem. Soc.* **2009**, *131*, 13833−13839.

(16) Xu, Z. P.; Stevenson, G.; Lu, C.-Q.; Lu, G. Q. Dispersion and Size Control of Layered Double Hydroxide Nanoparticles in Aqueous Solutions. *J. Phys. Chem. B* **2006**, *110*, 16923−16929.

(17) Gunjakar, J. L.; Kim, T. W.; Kim, H. N.; Kim, I. Y.; Hwang, S.-J. Mesoprous Layer-by-Layer Ordered Nanohybrids of Layered Double Hydroxide and Layered Metal Oxide: Highly Active Visible Light Photocatalysts with Improved Chemical Stability. *J. Am. Chem. Soc.* **2011**, *133*, 14998−15007.

(18) Hong, J.; Wang, Y.; Pan, J.; Zhong, Z.; Xu, R. Self-Assembled Dye-Layered Double Hydroxide-Pt Nanoparticles: A Novel H_2 Evolution System with Remarkable Enhanced Stability. *Nanoscale* **2011**, *3*, 4655−4661.

(19) Mohapatra, L.; Parida, K.; Satpathy, M. Molybdate/Tungstate Intercalated oxo-Bridged Zn/Y LDH for Solar Light Induced Photodegradation of Organic Pollutants. *J. Phys. Chem. C* **2012**, *116*, 13063−13070.

(20) Teramura, K.; Iguchi, S.; Mizuno, Y.; Shishido, T.; Tanaka, T. Photocatalytic Conversion of CO_2 in Water over Layered Double Hydroxides. *Angew. Chem., Int. Ed.* **2012**, *51*, 8008−8011.

(21) Choudary, B. M.; Madhi, S.; Chowdari, N. S.; Kantam, M. L.; Sreedhar, B. Layered Double Hydroxide Supported Nanopalladium Catalyst for Heck-, Suzuki-, Sonogashira-, and Stille-Type Coupling Reactions of Chloroarenes. *J. Am. Chem. Soc.* **2002**, *124*, 14127−14136.

(22) Basile, F.; Basini, L.; Fornasari, G.; Gazzano, M.; Trifirò, F.; Vaccari, A. New Hydrotalcite-Type Anionic Clays Containing Noble Metals. *Chem. Commun.* **1996**, 2435−2436.

(23) Takehira, K.; Shishido, T. Preparation of Supported Metal Catalysts Starting from Hydrotalcites as the Precursors and Their Improvements by Adopting "Memory Effect". *Catal. Surv. Asia* **2007**, *11*, 1−30.

(24) Beaudot, P.; De Roy, M. E.; Besse, J. P. Intercalation of Noble Metal Complexes in LDH Compounds. *J. Solid State Chem.* **2004**, *177*, 2691−2698.

(25) Varade, D.; Haraguchi, K. Efficient Approach for Preparing Gold Nanoparticles in Layered Double Hydroxide: Synthesis, Structure, and Properties. *J. Mater. Chem.* **2012**, *22*, 17649−17655.

(26) Zhao, J.; Kong, X.; Shi, W.; Shao, M.; Han, J.; Wei, M.; Evans, D. G.; Duan, X. Self-Assembly of Layered Double Hydroxide Nanosheets/Au Nanoparticles Ultrathin Films for Enzyme-Free Electrocatalysis of Glucose. *J. Mater. Chem.* **2011**, *21*, 13926−13933.

(27) Chmielarz, L.; Jabłońska, M.; Strumiński, A.; Piwowarska, Z.; Węgrzyn, A.; Witkowski, S.; Michalik, M. Selective Catalytic Oxidation of Ammonia to Nitrogen over Mg−Al, Cu−Mg−Al, and Fe−Mg−Al Mixed Metal Oxides Doped with Noble Metals. *Appl. Catal., B* **2013**, *130−131*, 152−162.

(28) Basile, F.; Fornasari, G.; Gazzano, M.; Vaccari, A. Synthesis and Thermal Evolution of Hydrotalcite-Type Compounds Containing Noble Metals. *Appl. Clay Sci.* **2000**, *16*, 185−200.

(29) Tsyganok, A. I.; Inaba, M.; Tsunoda, T.; Suzuki, K.; Takehira, K.; Hayakawa, T. Combined Partial Oxidation and Dry Reforming of Methane to Synthesis Gas over Noble Metals Supported on Mg−Al Mixed Oxide. *Appl. Catal., A* **2004**, *275*, 149−155.

(30) Parida, K. M.; Mohapatra, L. Cabonate Intercalated Zn/Fe Layered Double Hydroxide: A Novel Photocatalyst for the Enhanced Photo Degradation of Azo Dyes. *Chem. Eng. J.* **2012**, *179*, 131−139.

(31) Thomann, I.; Pinaud, B. A.; Chen, Z.; Clemens, B. M.; Jaramillo, T. F.; Brongersma, M. L. Plasmon Enhanced Solar-to-Fuel Energy Conversion. *Nano Lett.* **2011**, *11*, 3440−3446.

(32) Awazu, K.; Fujimaki, M.; Rockstuhl, C.; Tominaga, J.; Murakami, H.; Ohki, Y.; Yshida, N.; Watanabe, T. A Plasmonic Photocatalyst Consisting of Silver Nanoparticles Embedded in Titanium Dioxide. *J. Am. Chem. Soc.* **2008**, *120*, 1676−1680.